Supporting Information for

Multi-functional protective material with atomically dispersed zincophilic site enabling long-life zinc anode

Miaomiao Zhang,‡[a] Hongyu Wei,‡[a] Yitong Zhou,*[b] Wendong Wen,[a,c] Lin Zhang*[c] and Xin-Yao Yu*[a]

[a]School of Materials Science and Engineering, Anhui University, Hefei 230601, P. R. China.

[b]Institutes of Physical Science and Information Technology, Anhui University, Hefei 230601, P. R. China.

[c]Institute of Solid State Physics, Leibniz University Hannover, Hannover 30167, Germany.

Corresponding authors:

yuxinyao@ahu.edu.cn

lin.zhang@fkp.uni-hannover.de

zhouyt@ahu.edu.cn

Experimental Section

Materials

All the chemicals were of analytical reagent grade and used as received without any further treatment. Bismuth nitrate pentahydrate ($Bi(NO_3)_3 \cdot 5H_2O$), N, N-dimethylformamide (DMF), methanol, and ethanol were purchased from Sinopharm Chemical Reagent Co, Ltd (China). 1,3,5-benzenetricarboxylic acid (H_3BTC) were obtained from Aladdin (Shanghai, China). N-methyl pyrrolidone (>99.0%) were obtained from Macklin Reagent. The ultrapure water was prepared by using deionized water (DIW, 18.25 MΩ cm^{-1}).

Synthesis of the Bi-MOF

The preparation method for Bi-MOF is slightly modified from previous reports.[1] Initially, 0.3 mmol of $Bi(NO_3)_3 \cdot 5H_2O$ and 3.5 mmol of H_3BTC were dissolved in a mixture of 12 mL methanol and 48 mL DMF under continuous stirring. This mixture was then transferred into a 100 mL Teflon-lined autoclave and maintained at 120 °C for 24 hours. After naturally cooling to room temperature, the resulting precipitate (Bi-MOF) was collected by centrifugation at 8000 rpm, washed three times with methanol, and dried in a vacuum oven at 80 °C overnight.

Synthesis of the Bi SAs

The Bi-MOF precursors (0.1g) and dicyandiamide (0.6 g) were loaded separately into two porcelain boats with dicyandiamide in the up side and subjected to heating at 1000 °C for 2 hours under N_2, employing a gradual temperature ramp rate of 5 °C min^{-1}.

Synthesis of the NC

The as-prepared Bi-MOF precursor was first annealed at 1000 °C in N_2 atmosphere for 2 h. Then, the annealed product was mixed with a certain amount of dicyandiamide and annealed again at 1000 °C for 2 hours to obtain NC.

Synthesis of Metallic Bi Particles

30 mg of $Bi(NO_3)_3 \cdot 5H_2O$ was added into 20 mL of hydrazine hydrate (80%) and magnetically stirred at 80 °C for 4 h. The as-obtained material is metallic Bi particles.

Coating layers preparation

Commercial Zn foil (99.99% purity, 0.1 mm) and Ti foil (99.99% purity, 0.01 mm) were cleaned with ethanol before use. The coating materials and polyvinylidene fluoride (PVDF) binder were mixed in NMP solvent in a weight ratio of 8:2 to obtain a slurry. Coating layers were obtained by pouring of the as-obtained slurry onto Zn and Ti foils by means of a squeegee.

Synthesis of MnO_2

In a typical synthesis rocedure,[2] 50 mL of $K_2S_2O_8$ (0.1 M) was first mixed with 50 mL of $MnSO_4 \cdot 5H_2O$ (0.1 M). Next, 25 mL of NaOH (1.2 M) was added into the resulting solution and stirred for 1 h and then aged for another 1 h. The precipitate obtained was gathered, washed with water, and later freeze dried to obtain MnO_2.

Synthesis of $NH_4V_4O_{10}$

Initially, NH_4VO_3 (1.170 g) was dissolved in 35 mL of deionized water at 80 °C until complete dissolution. Subsequently, a slow addition of $H_2C_2O_4 \cdot 2H_2O$ (1.891 g) yielded a dark blue-green solution. This solution was then transferred to a 50 mL autoclave and subjected to heating at 140 °C for 48 hours. Afterward, the resulting material underwent washing with deionized water and ethanol, followed by vacuum drying at 80 °C for 12 h.[3]

Materials Characterization

The crystal structures were analyzed using high-power rotating target X-ray diffractometer (XRD, Smartlab). SEM images were acquired with a Zeiss Sigma 500 scanning electron microscope at an acceleration voltage of 5 kV. The inner morphologies were characterized by TEM and high-resolution TEM (JEM-2100F). HAADF-STEM images were performed with a JEOL JEM-2010 LaB6 operated at 200 kV. XPS data were collected using an ESCALAB250Xi spectrometer with an Al Kα light source. XAFS measurement and data analysis: XAFS spectra

at the Bi *L*-edge was collected at BL14W1 station in Shanghai synchrotron radiation facility (SSRF). The Bi *L*-edge XANES data were recorded in a fluorescence mode. Bi foil and Bi_2O_3 were used as reference. The elemental content of Bi was analyzed with ICP-OES (iCAP 7400). The SECM images were recorded on an electrochemical scanning microscope (Aptar Switzerland). The deposition behavior of Zn^{2+} on the Zn electrodes was monitored in real time using an YM710TR optical microscope.

Electrochemical Measurements

CR2032 coin cells were assembled for electrochemical experiments by using Glass fiber filter (GF, Whatman) as the separator and 2 M $ZnSO_4$ as electrolyte. Galvanostatic charge and discharge tests were executed using NEWARE CT4008TN battery testers. CV curves, chronoamperometry (CA), and EIS tests were performed on Biologic electrochemical workstation (MPG-2). LSV curves and Tafel plots were recorded on an electrochemical station (CHI660E, China). Zn//MnO_2 full cells were assembled with 2 M $ZnSO_4$ and 0.2 M $MnSO_4$ as electrolytes.

The Zn^{2+} migration number ($t_{Zn^{2+}}$) is calculated by Bruce-Vincent method:

$$t_{Zn^{2+}} = \frac{I_S(\Delta V - I_0R_0)}{I_0(\Delta V - I_SR_S)}$$

Where I_0 and R_0 is the initial current and resistance, respectively; I_s and R_s is the steady-state current and resistance, respectively. ΔV is the applied voltage (25 mV).

The activation energy (E_a) is calculated according to the Arrhenius equation:

$$\frac{1}{R_{ct}} = A \exp\left(\frac{-E_a}{RT}\right)$$

Where R_{ct} is the charge-transfer resistance, A is the pre-exponential factor, R is the gas constant, and T is the temperature.

The exchange current density is calculated by the Butler-Volmer approximation equation:

$$i = i_0\frac{2F}{RT}\eta$$

Where i is the current density, i_0 is the exchange current density, η is the overpotential, F is the Faraday constant, R is the gas constant, and T is the temperature, respectively.

Ionic conductivity is calculated through the following equation:

$$\delta = \frac{L}{SR_b}$$

Where L is the thickness of the coating, S is the contact area, and R_b is resistance according to the EIS measurements.

COMSOL Calculations

The physics modules "Tertiary Current Distribution" and "Nernst-Planck" in COMSOL Multiphysics 6.1 were employed for simulations using the Finite Element Method (FEM).[4] These simulations aimed to model the electric field distribution and Zn^{2+} flux during charging. The reaction kinetics of all electrodes were described using the Butler-Volmer expression, while the flux of each ion was calculated using the Nernst-Planck equation. Additionally, insulated boundaries were assumed for the vertical walls. For computational efficiency, only the cathode was considered as a deformable boundary, and refined grid settings were used to ensure accurate simulation. The simulation focused on the initial 10 seconds of the battery charging process.

DFT Calculations

All the DFT calculations were performed by Vienna Ab-initio Simulation Package (VASP).[5-7] The Perdew-Burke-Ernzerh (PBE) in the generalized gradient approximation (GGA) was applied to describe the exchange-correlation function.[8, 9] Based on the plane wave method, the projector augmented-wave (PAW) method with an energy cutoff of 400 eV was implemented for the electron-ion interactions.[10, 11] The van der Waals interaction was taken into account using DFT-D3 method with Becke-Jonson damping dispersion correction. All structures were fully relaxed until the electronic energy and force acting on atom were smaller than 10^{-4} eV and 0.02 eV·$Å^{-1}$, respectively. The Brillouin-zone sampling was conducted using Monkhorst-Pack

(MP) grids of special points with the separation of 0.04 $Å^{-1}$. A Gaussian smearing of 0.05 eV was applied to speed up self-consistent field iteration. The optimized structures were illustrated with VESTA software.[12]

The chemical potential of Zn (μ_{Zn}) was calculated through the following equation:

$$\mu_{Zn} = \frac{(E_{total} - E_{surface} - N * E_{Zn})}{N}$$

Where E_{total}, $E_{surface}$, and E_{Zn} are the DFT calculated energies of the surfaces with deposited Zn atoms, a clean surface, and an atom in bulk Zn, respectively. *N* is the number of Zn atoms deposited on the surface.

Supplementary Figures

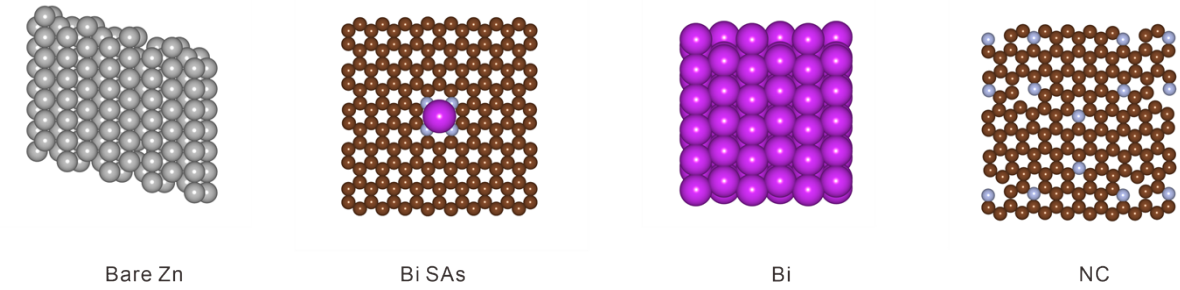

Figure S1. Structural models of (a) Zn, (b) Bi SAs. (c) Bi, and (d) NC. The gray, purple, cyan and dark brown balls represent Zn, Bi, N, and C elements, respectively.

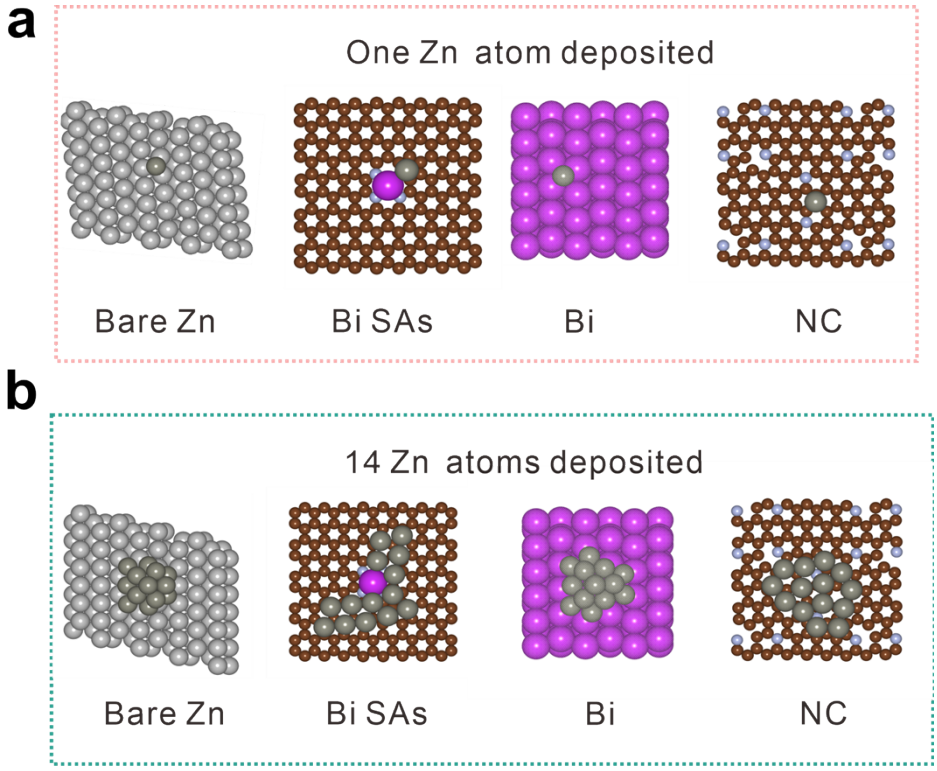

Figure S2. (a) One Zn atom deposited and (b) 14 Zn atoms deposited on bare Zn, Bi SAs, Bi, and NC. The gray, purple, cyan, dark brown, and dark gray balls represent Zn, Bi, N, C elements and deposited Zn. respectively.

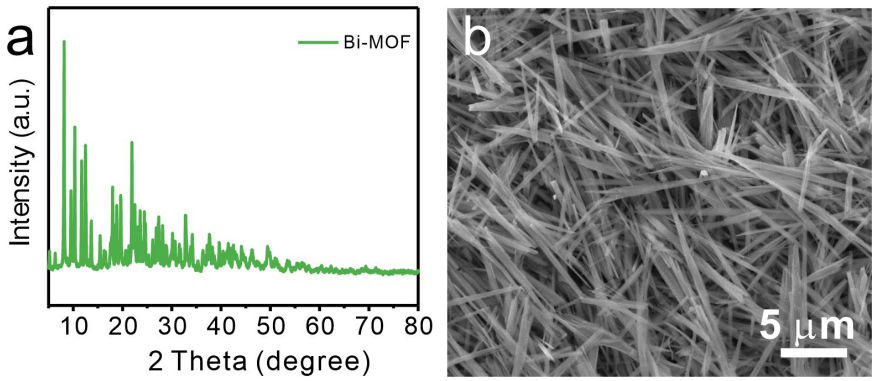

Figure S3. (a) XRD pattern and (b) SEM image of Bi-MOF.

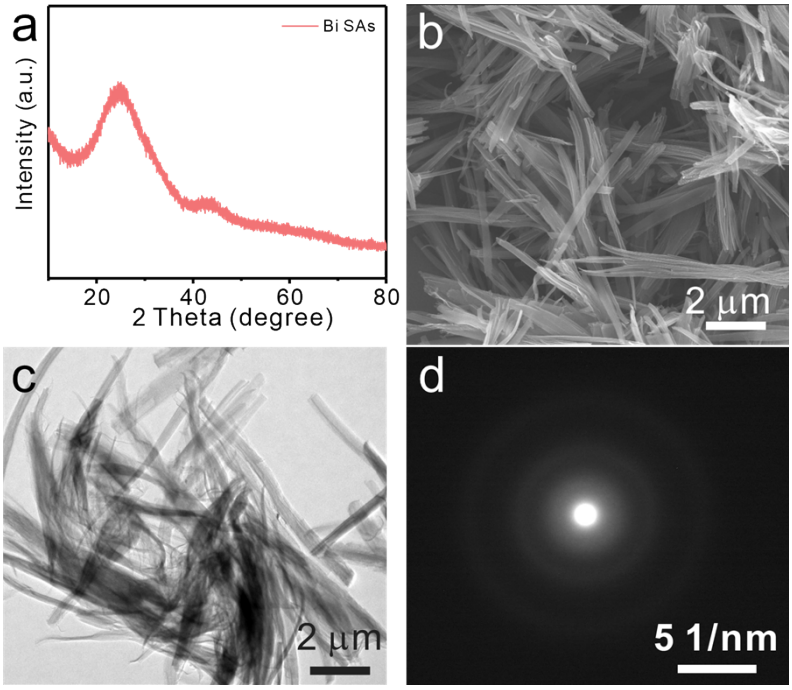

Figure S4. (a) XRD pattern, (b) SEM image, (c) TEM image, and (d) SAED pattern of Bi SAs.

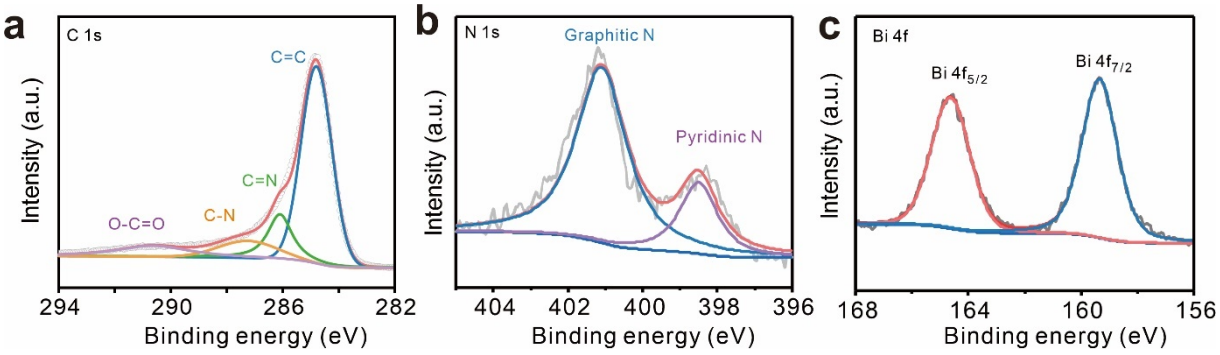

Figure S5. High-resolution (a) C 1s, (b) N 1s, and (c) Bi 4f XPS spectra of Bi SAs.

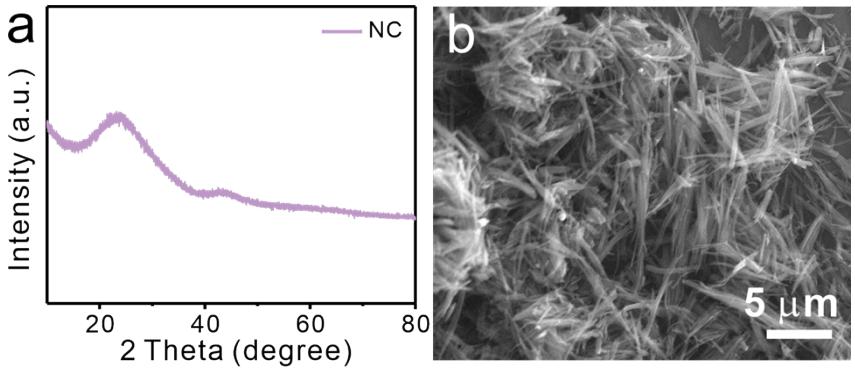

Figure S6. (a) XRD pattern and (b) SEM image of NC.

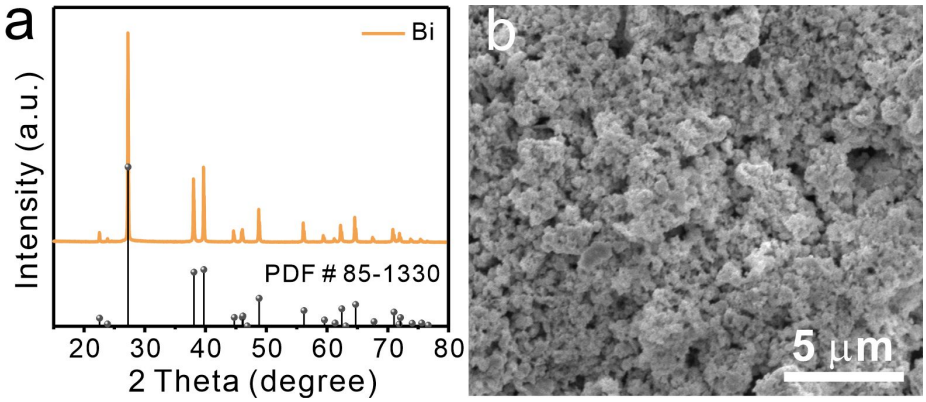

Figure S7. (a) XRD pattern and (b) SEM image of metallic Bi particles.

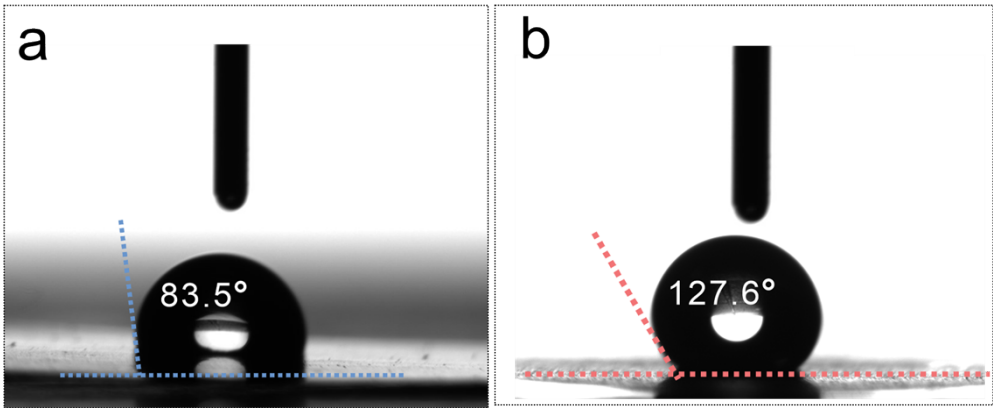

Figure S8. The contact angles of (a) bare Zn and (b) Bi SAs@Zn.

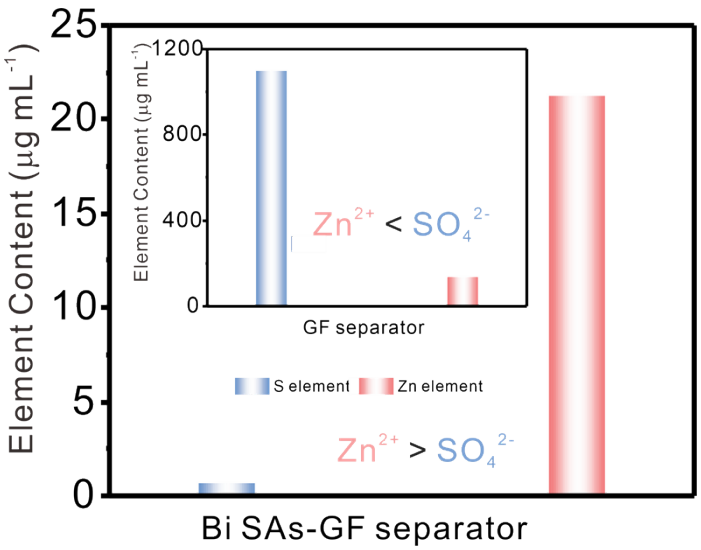

Figure S9. Zn^{2+} and SO_4^{2-} permeability test of Bi SAs/NC-GF and GF (inset) membranes.

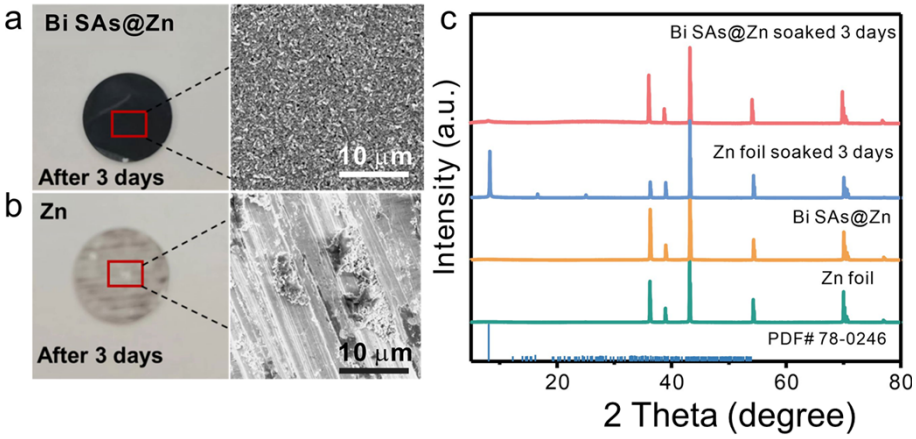

Figure S10. Top-view digital photos and SEM images of (a,b) Bi SAs@Zn and bare Zn anodes after immersion in 2 M $ZnSO_4$ electrolyte for 3 days and the corresponding (c) XRD patterns.

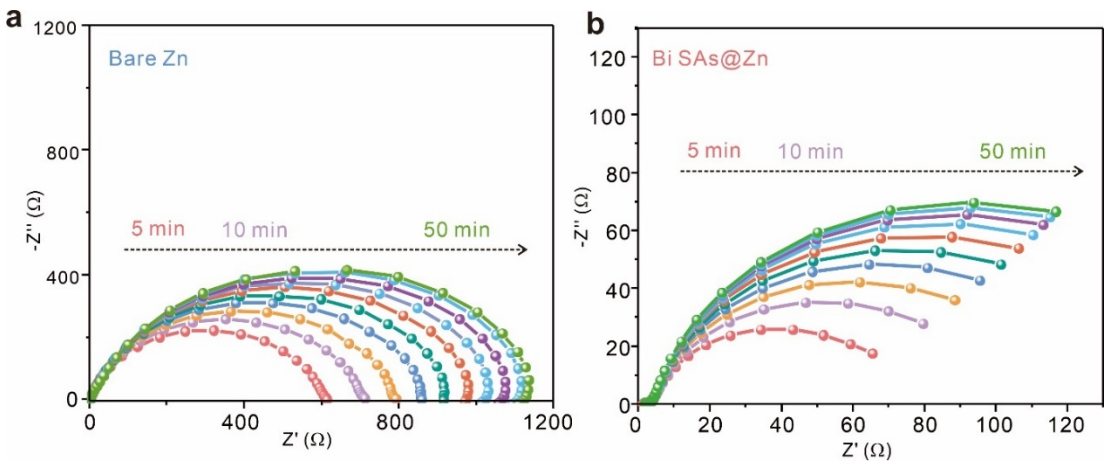

Figure S11. Operando EIS evolution of (a) bare Zn//bare Zn and (b) Bi SAs@Zn//Bi SAs@Zn symmetric cells. The EIS measurements were performed after Zn rested for 5 min. The total Zn deposition time is 50 min.

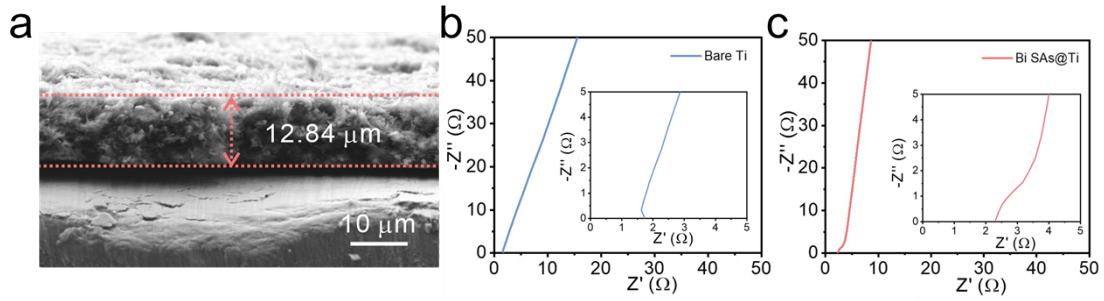

Figure S12. (a) Cross-section SEM image of Bi SAs layer. EIS plots of (b) Bare Ti//Bare Ti and (c) Bi SAs@Ti//Bi SAs@Ti symmetrical cells. The inset is the enlargement of the data in the range of 0~5 Ω.

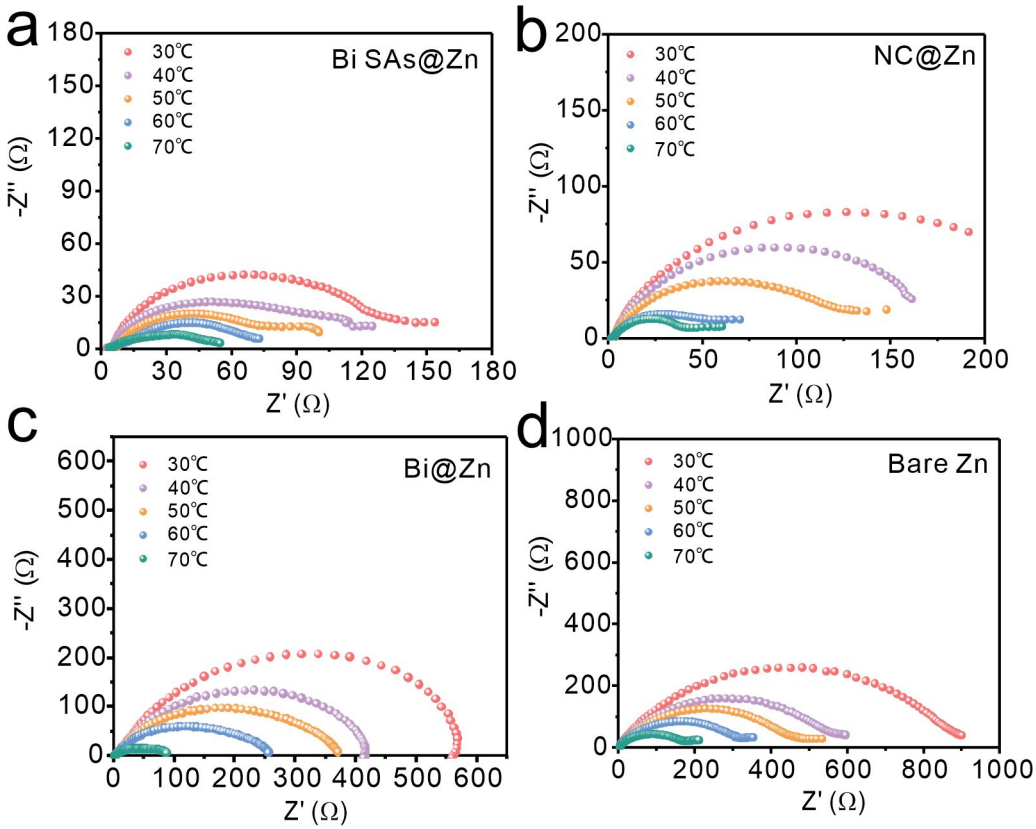

Figure S13. EIS plots of (a) Bi SAs@Zn, (b) NC@Zn, (c) Bi@Zn, and (d) bare Zn symmetric cells at different temperatures.

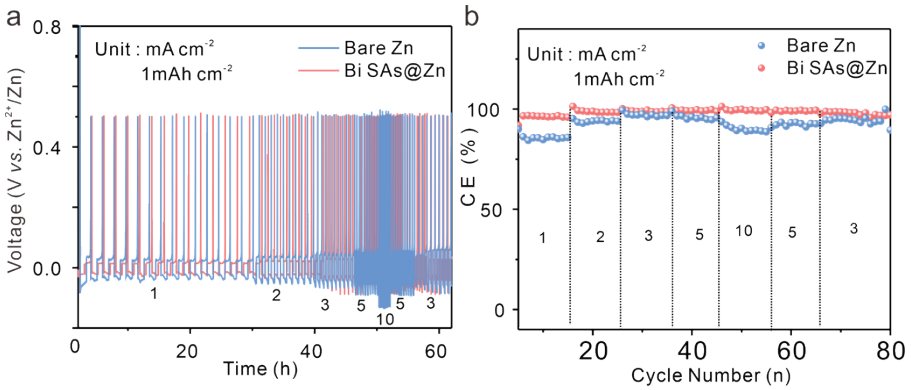

Figure S14. (a) Comparison of voltage profiles and (b) CE profiles of the asymmetric bare Zn//Ti and Bi SAs@Zn//Ti cells at the various current density ranging from 1 to 10 mA cm^{-2}.

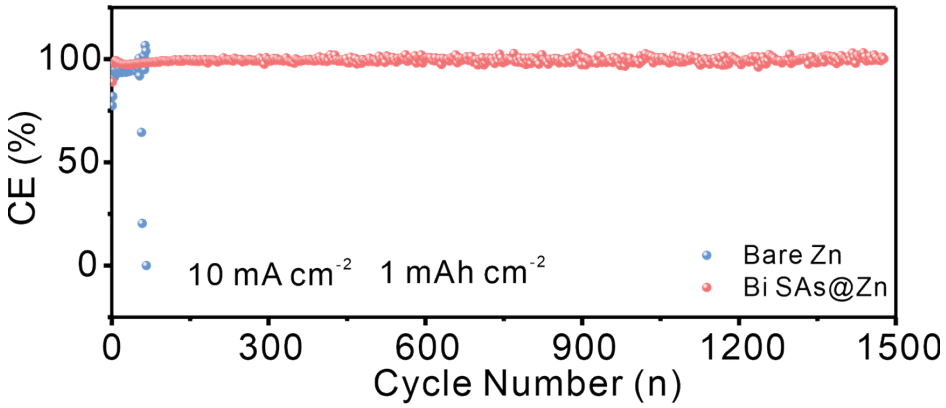

Figure S15. CE of the asymmetric bare Zn//Ti and Bi SAs@Zn//Ti cells at 10 mA cm^{-2}/1 mAh cm^{-2}.

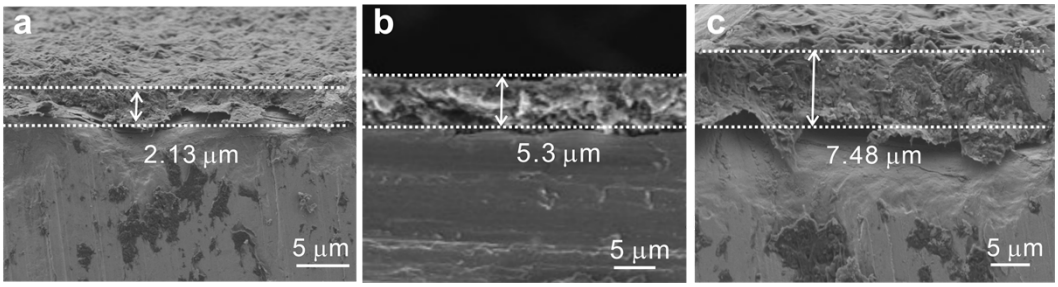

Figure S16. The cross-sectional SEM images of Bi SAs layers with different thickness: (a) Bi SAs@Zn-1, (b) Bi SAs@Zn, and (c) Bi SAs@Zn-2.

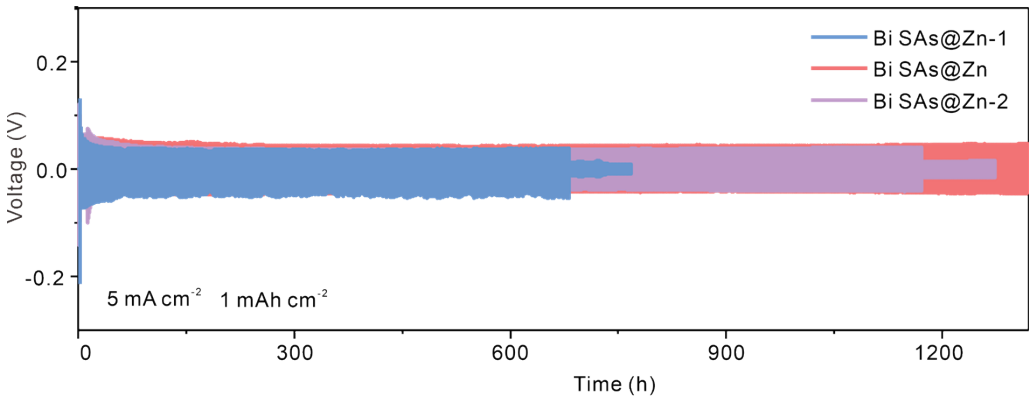

Figure S17. Discharge and charge voltage profiles of Bi SAs@Zn-1, Bi SAs@Zn and Bi SAs@Zn-2 symmetric cells at 5 mA cm^{-2}/1 mAh cm^{-2}.

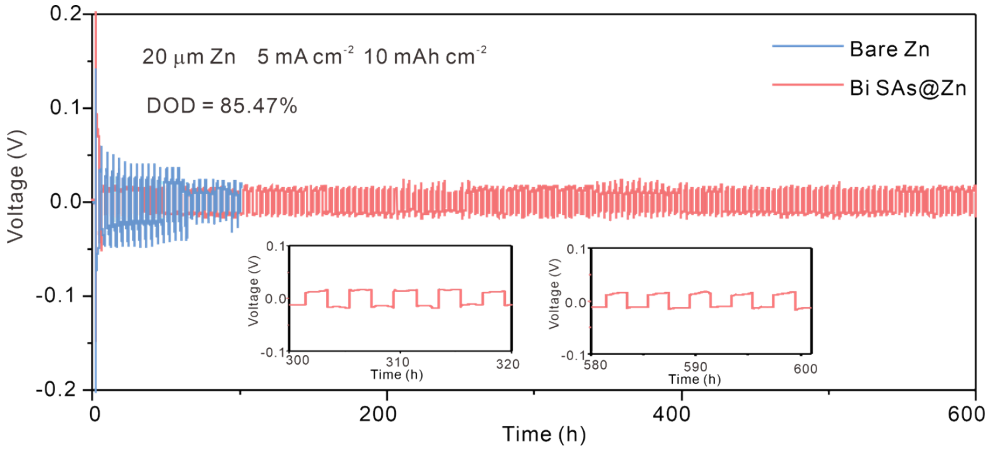

Figure S18. Cyclic performance of the symmetric cells with bare Zn and Bi SAs@Zn at 5 mA cm^{-2} and 10 mAh cm^{-2} with 85.47% of DOD (Thickness of Zn: 20 μm).

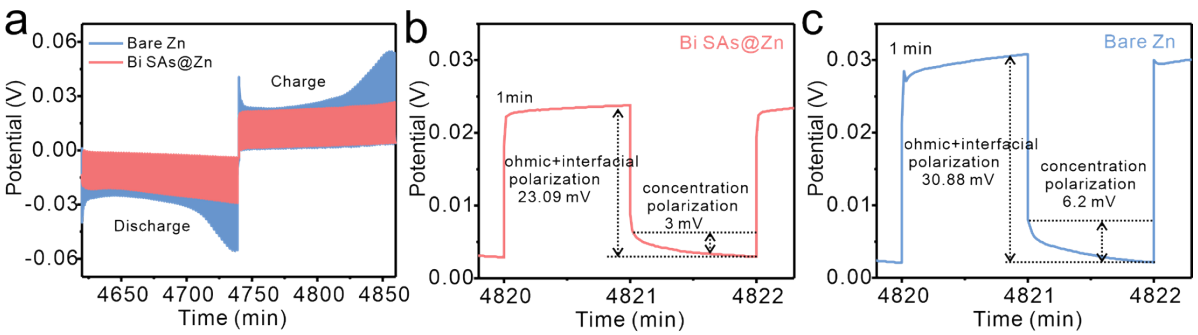

Figure S19. (a) GITT curves of bare Zn and Bi SAs@Zn. (b,c) The partial enlargement of GITT curves for (b) Bi SAs@Zn and (c) bare Zn.

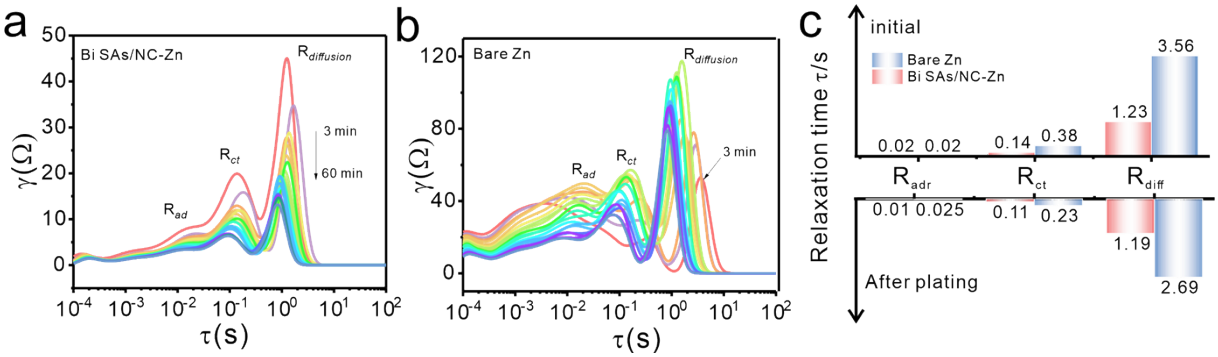

Figure S20. DRT curves of (a) Bi SAs@Zn//Bi SAs@Zn and (b) Bare Zn//Bare Zn during Zn deposition at 1 mA cm^{-2} for 3 min and rested for 3 min. (c) The comparation of relaxation time (τ) changes of diverse interfacial process.

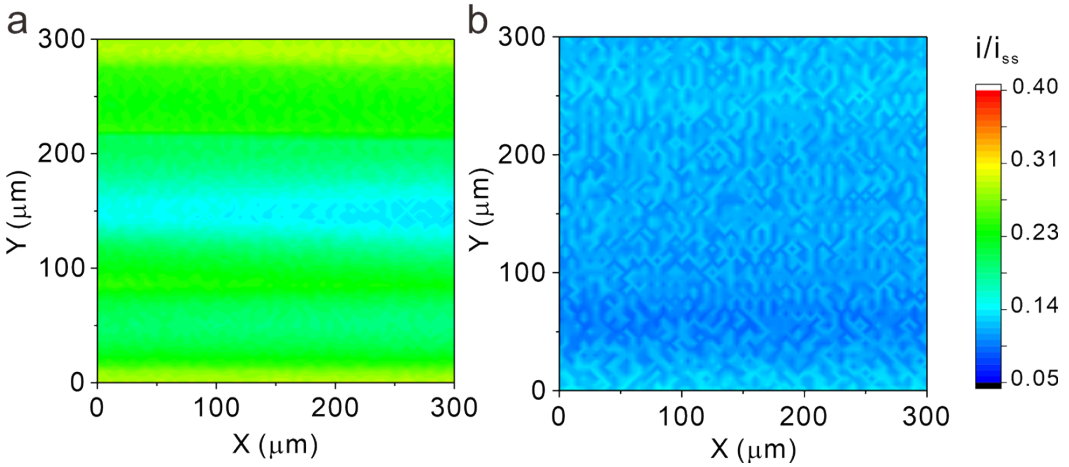

Figure S21. SECM images of (a) bare Zn surface and (b) Bi SAs@Zn anode before Zn deposition.

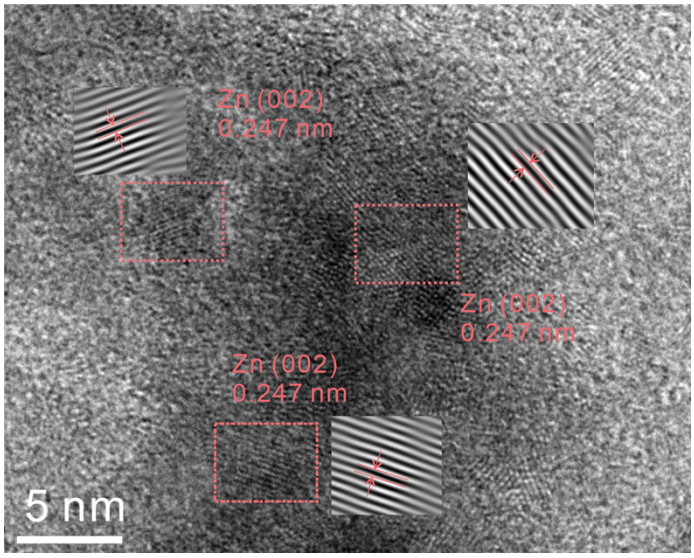

Figure S22. HRTEM images of the Bi SAs surface after zinc deposition for 600 s at 5 mA cm^{-2}.

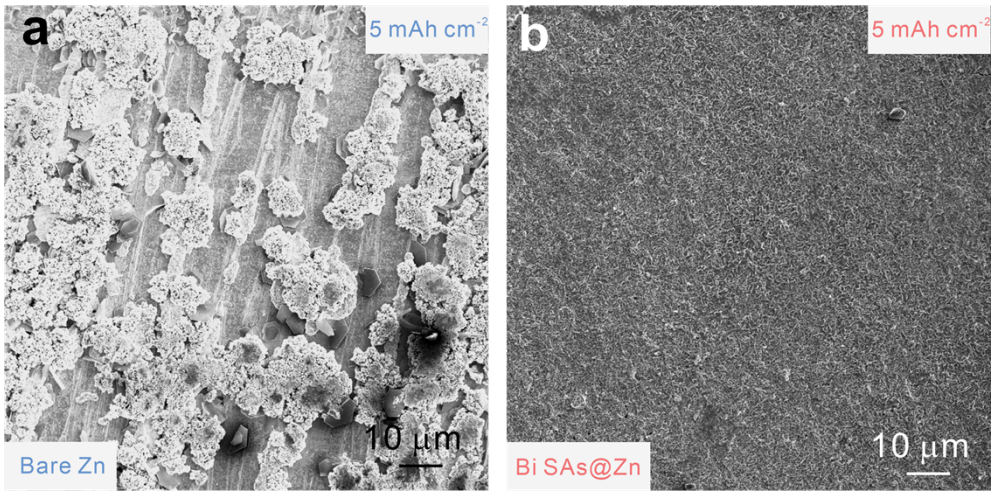

Figure S23. SEM images of (a) bare Zn and (b) Bi SAs@Zn after zinc plating at 5 mAh cm^{-2}.

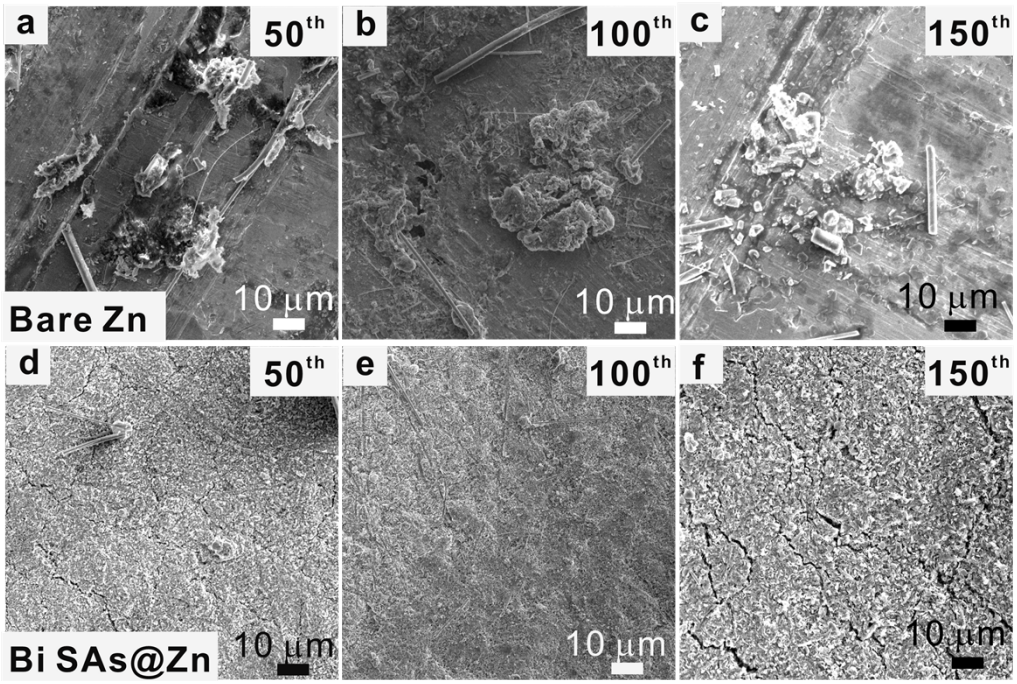

Figure S24. Top view SEM images of (a-c) bare Zn and (d-f) Bi SAs@Zn anodes after different cycles at 5 mA cm^{-2} and 1 mAh cm^{-2}.

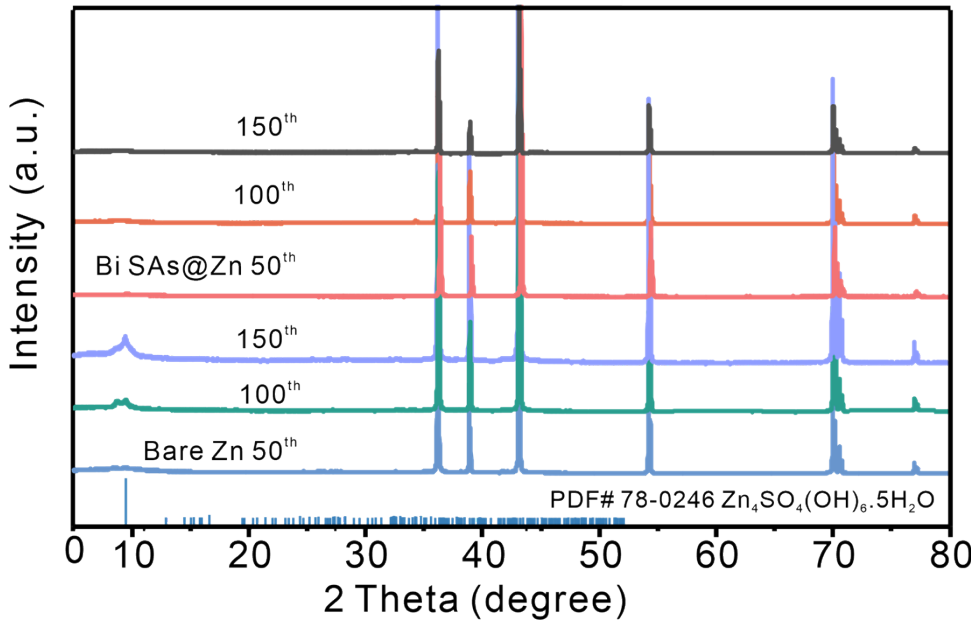

Figure S25. XRD patterns of bare Zn and Bi SAs@Zn anodes after different cycles at 5 mA cm^{-2} and 1 mAh cm^{-2}.

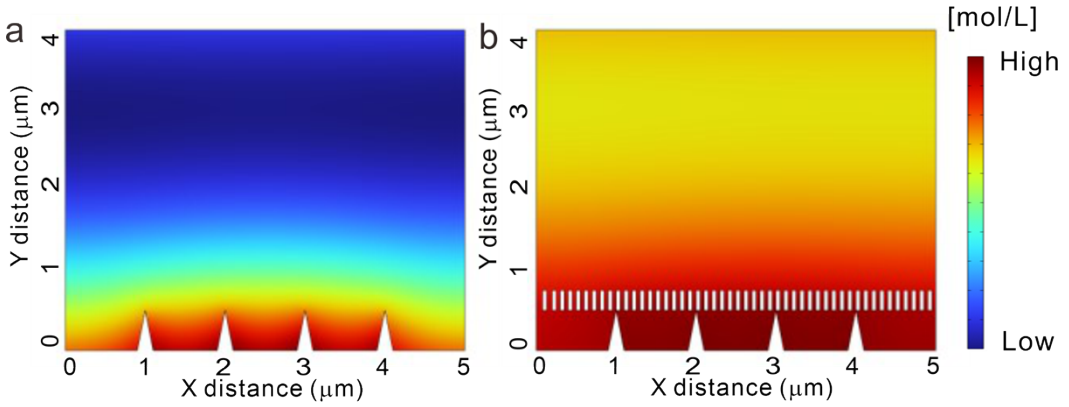

Figure S26. COMSOL simulations of Zn^{2+} flux for (a) bare Zn and (b) Bi SAs@Zn.

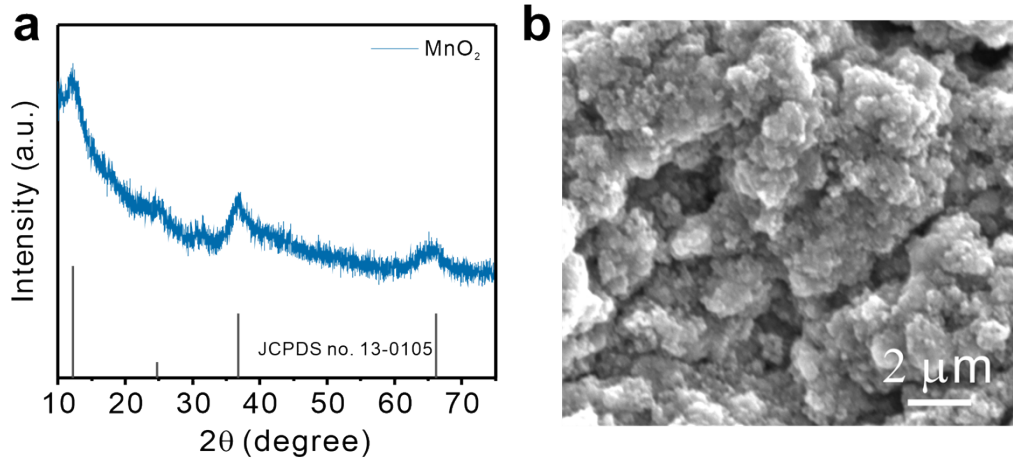

Figure S27. (a) XRD pattern and (b) SEM image of MnO_2.

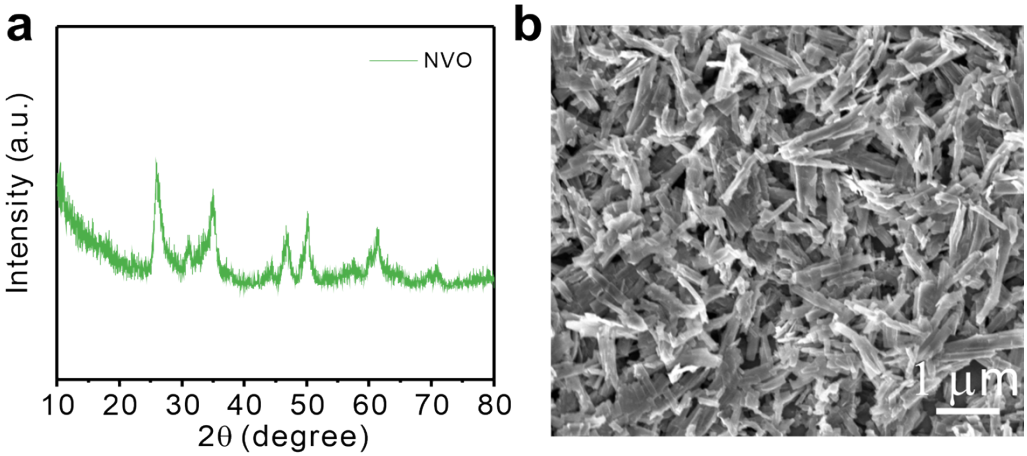

Figure S28. (a) XRD pattern and (b) SEM image of $NH_4V_4O_{10}$.

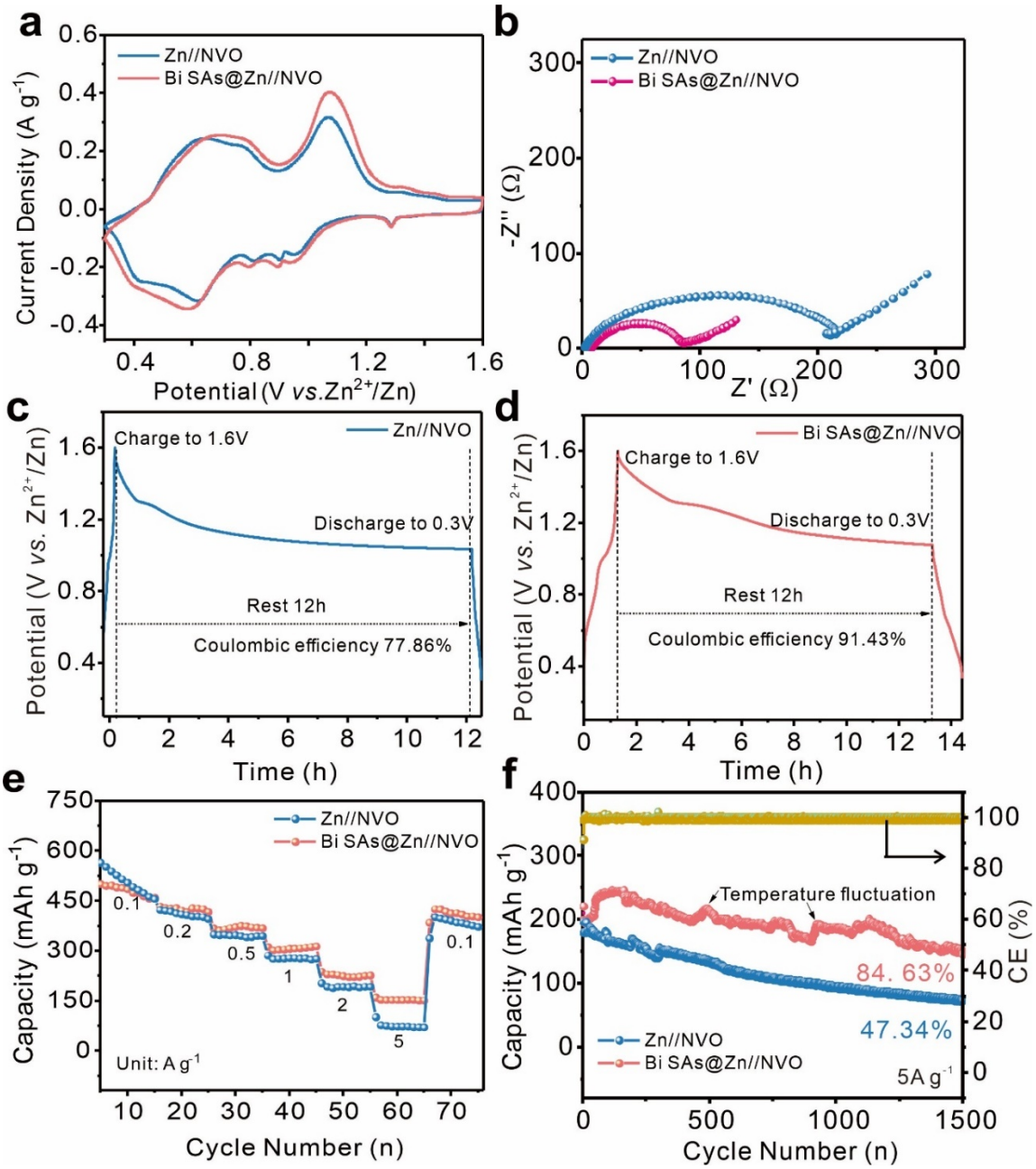

Figure S29. (a) CV curves, (b) EIS plots before cycling, (e) Rate performance, and (f) Cycling performance of Zn/NVO and Bi SAs@Zn//NVO full cells at 5 A g^{-1}. Self-discharging voltage–time curves of (c) Zn/NVO and (d) Bi SAs@Zn//NVO full cells.

Table S1. FT-EXAFS fitting parameters at the Bi L_3-edge. (S_0^2=0.82)

Sample	Scattering pair	CN	*R* (Å)	σ^2 (10^{-3} Å^2)	ΔE_0 (eV)	*R* factor
Bi SAs	Bi-N	3.8	2.01	5.2	1.5	0.02

CN, the coordination numbers; *R*, distance between absorber and backscatter atoms; σ_2, Debye-Waller factor; ΔE_0 is edge-energy shift; *R* factor is used to evaluate the degree of fitting. This value was fixed during EXAFS fitting. Error bounds that characterize the structural parameters obtained by EXAFS spectroscopy were estimated as N ± 20%; *R* ± 1%; σ_2 ± 20%; ΔE_0 ± 20%.

Table S2. Performance comparison of recently reported symmetric cell with modified zinc anode.

Anode	Electrolyte	Current density (mA cm^{-2})	Capacity (mAh cm^{-2})	Cumulative Capacity (mAh cm^{-2})	Cycle life (h)	Refs.
Bi SAs@Zn	**2 M $ZnSO_4$**	**5**	**1**	**10500**	**4200**	**This**
Bi SAs@Zn	**2 M $ZnSO_4$**	**20**	**5**	**6000**	**600**	**work**
SA-Zn/CN@Zn	2 M $ZnSO_4$	1	1	1650	3300	[13]
Sn NC@Zn	2 M $ZnSO_4$	1	1	500	1000	[14]
ND@Zn	2 M $ZnSO_4$	1	0.5	2010	4020	[15]
ZnO/C-Zn	2 M $ZnSO_4$	5	1	1700	680	[16]
g-C_3N4@Zn	2 M ZnSO4	1	0.5	500	1000	[17]
CN-Zn	2 M $ZnSO_4$	1	1	650	1300	[18]
CCF-K@Zn	1 M $Zn(OTf)_2$	1	1	2500	5000	[19]
G@Zn	2 M ZnSO4	0.1	0.1	10	200	[20]
NGO@Zn	2 M ZnSO4	1	1	600	1200	[21]
C-750@Zn	2 M ZnSO4	5	5	1000	400	[22]
Ti-Zn	2 M $ZnSO_4$	2	2	2200	1100	[23]
ZnTe@Zn	2 M $ZnSO_4$	1	0.5	1650	3300	[24]
Bi@Zn	2 M $ZnSO_4$	2	1	1700	1700	[25]
PSN-Zn	2 M $ZnSO_4$	1	1	400	800	[26]
ZrO_2@Zn	2 M $ZnSO_4$	1	1	3000	6000	[27]
Bi/Bi_2O_3@Zn	2 M $ZnSO_4$	1	1	1500	3000	[28]

Table S3 Comparison of typical parameters for our work with recently reported Zn-based full cells.

Anode	Cathode	Electrolyte	Final capacity (mAh g^{-1})	Capacity retention (%)	Current density (mAh g^{-1})	References
Bi SAs@Zn	**MnO_2**	**2 M $ZnSO_4$ + 0.2 M $MnSO_4$**	**150.95**	**95.58% after 1000 cycles**	**1000**	**This work**
FCOF@Zn	MnO_2	2 M $ZnSO_4$ + 0.2 M $MnSO_4$	130	92% after 1000 cycles	1000	[29]
SA@Zn	V_2O_5	3 M $ZnSO_4$	150	92% after 2700 cycles	1000	[30]
ZIF/Zn	MnO_2	3 M $ZnSO_4$	119.6	80.3% after 300 cycles	1000	[31]
ZWO@Zn	V_6O_{13}	2 M $ZnSO_4$	204	80% after 1000 cycles	1000	[32]
Zn@PANI	MnO_2	2 M $ZnSO_4$ + 0.1 M $MnSO_4$	134	94.3% after 1000 cycles	1000	[33]
NFZP@Zn	MnO_2	1 M $ZnSO_4$ + 0.1 M $MnSO_4$	90.0	72.8% after 500 cycles	800	[34]
ZnSe@Zn	MnO_2	2 M $ZnSO_4$ + 0.1 M $MnSO_4$	100.0	36.0% after 1800 cycles	600	[35]

References

1 E. Zhang, T. Wang, K. Yu, J. Liu, W. Chen, A. Li, H. Rong, R. Lin, S. Ji, X. Zheng, Y. Wang, L. Zheng, C. Chen, D. Wang, J. Zhang and Y. Li, Bismuth Single Atoms Resulting from Transformation of Metal–Organic Frameworks and Their Use as Electrocatalysts for CO_2 Reduction, *J. Am. Chem. Soc.*, 2019, **141**, 16569-16573.

2 T. Xiong, Z. G. Yu, H. Wu, Y. Du, Q. Xie, J. Chen, Y.-W. Zhang, S. J. Pennycook, W. S. V. Lee and J. Xue, Defect Engineering of Oxygen-Deficient Manganese Oxide to Achieve High-Performing Aqueous Zinc Ion Battery, *Adv. Energy Mater.*, 2019, **9**, 1803815.

3 D. Li, Y. Tang, S. Liang, B. Lu, G. Chen and J. Zhou, Self-assembled multilayers direct a buffer interphase for long-life aqueous zinc-ion batteries, *Energy Environ. Sci.*, 2023, **16**, 3381-3390.

4 M. Liu, W. Yuan, G. Ma, K. Qiu, X. Nie, Y. Liu, S. Shen and N. Zhang, In-Situ Integration of a Hydrophobic and Fast-Zn2+-Conductive Inorganic Interphase to Stabilize Zn Metal Anodes, *Angew. Chem., Int. Ed.*, 2023, **62**, e202304444.

5 G. Kresse and J. Hafner, Ab initio molecular dynamics for liquid metals, *Physical Review B*, 1993, **47**, 558-561.

6 G. Kresse and J. Furthmüller, Efficient iterative schemes for ab initio total-energy calculations using a plane-wave basis set, *Physical Review B*, 1996, **54**, 11169-11186.

7 G. Kresse and J. Furthmüller, Efficiency of ab-initio total energy calculations for metals and semiconductors using a plane-wave basis set, *Comput. Mater. Sci*, 1996, **6**, 15-50.

8 J. P. Perdew and Y. Wang, Accurate and simple analytic representation of the electron-gas correlation energy, *Physical Review B*, 1992, **45**, 13244-13249.

9 J. P. Perdew, K. Burke and M. Ernzerhof, Generalized Gradient Approximation Made Simple, *Phys. Rev. Lett.*, 1996, **77**, 3865-3868.

10 P. E. Blöchl, Projector augmented-wave method, *Physical Review B*, 1994, **50**, 17953-17979.

11 G. Kresse and D. Joubert, From ultrasoft pseudopotentials to the projector augmented-wave method, *Physical Review B*, 1999, **59**, 1758-1775.

12 K. Momma and F. Izumi, VESTA 3 for three-dimensional visualization of crystal, volumetric and morphology data, *J. Appl. Crystallogr.*, 2011, **44**, 1272-1276.

13 Z. Cao, R. Ma, X. Xiao, D. Xiong, W. Yi, S. Tao, Z. Song, Y. Xiong, W. Deng, J. Hu, H. Hou, X. Ji and G. Zou, Single atom vacancy engineering with highly reversible N4 sites enable ultra-low overpotential for durable zinc-ion supercapacitors, *Energy Storage Mater.*, 2024, **66**, 103189.

14 Y. Wang, Y. Tan and C. Cheng, Atomic Sn sites on nitrogen-doped carbon as a zincophilic and hydrophobic protection layer for stable Zn anodes, *J. Mater. Chem. A*, 2024, **12**, 428-439.

15 M. Wang, J. Zhang, M. Wu, D. Yang, P. Sun, J. Sun, Z. Zhang, X. Chen, J. Ba, Y. Wang, J. Qiu and Y. Wei, Nanodiamond Implanted Zinc Metal Anode for Long-Life Aqueous Zinc Ion Batteries, *Adv. Funct. Mater.*, 2024, **n/a**, 2315757.

16 W. Deng, N. Zhang and X. Wang, Hybrid interlayer enables dendrite-free and deposition-modulated zinc anodes, *Chem. Eng. J.*, 2022, **432**, 134378.

17 J. Jiang, Z. Pan, J. Yuan, J. Shan, C. Chen, S. Li, HaiXu, Y. Chen, Q. Zhuang, Z. Ju, H. Dou, X. Zhang and J. Wang, Zincophilic polymer semiconductor as multifunctional

protective layer enables Dendrite-Free zinc metal anodes, *Chem. Eng. J.*, 2023, **452**, 139335.

18 X. Wang, K. Yang, C. Ma, W. Lu, N. Chen, M. Yao, Z. Li, C. Liu, H. Yue, D. Zhang and F. Du, N-Rich carbon as Zn2+ modulation layers for dendrite-free, highly reversible zinc anodes, *Chem. Eng. J.*, 2023, **452**, 139257.

19 R. E. A. Ardhi, G. Liu, J. Park and J. K. Lee, Alkali Adatom-amplified Schottky contact and built-in voltage for stable Zn-metal anodes, *Energy Storage Mater.*, 2023, **54**, 863-874.

20 Z. Li, L. Wu, S. Dong, T. Xu, S. Li, Y. An, J. Jiang and X. Zhang, Pencil Drawing Stable Interface for Reversible and Durable Aqueous Zinc-Ion Batteries, *Adv. Funct. Mater.*, 2021, **31**, 2006495.

21 J. Zhou, M. Xie, F. Wu, Y. Mei, Y. Hao, R. Huang, G. Wei, A. Liu, L. Li and R. Chen, Ultrathin Surface Coating of Nitrogen-Doped Graphene Enables Stable Zinc Anodes for Aqueous Zinc-Ion Batteries, *Adv. Mater.*, 2021, **33**, 2101649.

22 R. Yuksel, O. Buyukcakir, W. K. Seong and R. S. Ruoff, Metal-Organic Framework Integrated Anodes for Aqueous Zinc-Ion Batteries, *Adv. Energy Mater.*, 2020, **10**, 1904215.

23 Y. Zhao, S. Guo, M. Chen, B. Lu, X. Zhang, S. Liang and J. Zhou, Tailoring grain boundary stability of zinc-titanium alloy for long-lasting aqueous zinc batteries, *Nat. Commun.*, 2023, **14**, 7080.

24 R. Wang, S. Xin, D. Chao, Z. Liu, J. Wan, P. Xiong, Q. Luo, K. Hua, J. Hao and C. Zhang, Fast and Regulated Zinc Deposition in a Semiconductor Substrate toward High-Performance Aqueous Rechargeable Batteries, *Adv. Funct. Mater.*, 2022, **32**, 2207751.

25 R. Zhao, X. Dong, P. Liang, H. Li, T. Zhang, W. Zhou, B. Wang, Z. Yang, X. Wang, L. Wang, Z. Sun, F. Bu, Z. Zhao, W. Li, D. Zhao and D. Chao, Prioritizing Hetero-Metallic Interfaces via Thermodynamics Inertia and Kinetics Zincophilia Metrics for Tough Zn-Based Aqueous Batteries, *Adv. Mater.*, 2023, **35**, 2209288.

26 S. Zhou, Y. Wang, H. Lu, Y. Zhang, C. Fu, I. Usman, Z. Liu, M. Feng, G. Fang, X. Cao, S. Liang and A. Pan, Anti-Corrosive and Zn-Ion-Regulating Composite Interlayer Enabling Long-Life Zn Metal Anodes, *Adv. Funct. Mater.*, 2021, **31**, 2104361.

27 B. Wei, J. Zheng, Abhishek, X. Liu, J. Wu, Z. Qi, Z. Hou, R. Wang, J. Ma, A. N. Gandi, Z. Wang and H. Liang, Design Principle of Insulating Surface Protective Layers for Metallic Zn Anodes: A Case Study of ZrO2, *Adv. Energy Mater.*, 2024, **n/a**, 2401018.

28 X. Tian, Q. Zhao, M. Zhou, X. Huang, Y. Sun, X. Duan, L. Zhang, H. Li, D. Su, B. Jia and T. Ma, Synergy of Dendrites-Impeded Atomic Clusters Dissociation and Side

Reactions Suppressed Inert Interface Protection for Ultrastable Zn Anode, *Adv. Mater.*, 2024, **36**, 2400237.

29 Z. Zhao, R. Wang, C. Peng, W. Chen, T. Wu, B. Hu, W. Weng, Y. Yao, J. Zeng, Z. Chen, P. Liu, Y. Liu, G. Li, J. Guo, H. Lu and Z. Guo, Horizontally arranged zinc platelet electrodeposits modulated by fluorinated covalent organic framework film for high-rate and durable aqueous zinc ion batteries, *Nat. Commun.*, 2021, **12**, 6606.

30 M. Fu, H. Yu, S. Huang, Q. Li, B. Qu, L. Zhou, G.-C. Kuang, Y. Chen and L. Chen, Building Sustainable Saturated Fatty Acid-Zinc Interfacial Layer toward Ultra-Stable Zinc Metal Anodes, *Nano Lett.*, 2023, **23**, 3573-3581.

31 X. Liu, F. Yang, W. Xu, Y. Zeng, J. He and X. Lu, Zeolitic Imidazolate Frameworks as Zn^{2+} Modulation Layers to Enable Dendrite-Free Zn Anodes, *Adv. Sci.*, 2020, **7**, 2002173.

32 C. Yi, L. Jiao, J. Wang, Y. Ma, H. Bai, Q. Liu, S. Wang, W. Xin, Y. Lei, T. Zhang, L. Yang, D. Shu, S. Yang, K. Li, C. Li, H. Li, W. Zhang and B. Cheng, Multi-Scale Functionally Designed ZnWO4 Artificial Interphase for Ultra-Stable Aqueous Zn Metal Anodes Under High Current Rates, *Adv. Funct. Mater.*, 2024, **n/a**, 2404579.

33 B. Li, S. Liu, Y. Geng, C. Mao, L. Dai, L. Wang, S. C. Jun, B. Lu, Z. He and J. Zhou, Achieving Stable Zinc Metal Anode Via Polyaniline Interface Regulation of Zn Ion Flux and Desolvation, *Adv. Funct. Mater.*, 2024, **34**, 2214033.

34 S. Wang, Z. Yang, B. Chen, H. Zhou, S. Wan, L. Hu, M. Qiu, L. Qie and Y. Yu, A highly reversible, dendrite-free zinc metal anodes enabled by a dual-layered interface, *Energy Storage Mater.*, 2022, **47**, 491-499.

35 L. Zhang, B. Zhang, T. Zhang, T. Li, T. Shi, W. Li, T. Shen, X. Huang, J. Xu, X. Zhang, Z. Wang and Y. Hou, Eliminating Dendrites and Side Reactions via a Multifunctional ZnSe Protective Layer toward Advanced Aqueous Zn Metal Batteries, *Adv. Funct. Mater.*, 2021, **31**, 2100186.